

# Effects of correlated magnetic noises from shared control lines on two-qubit gate

Yinan Fang<sup>1,2\*</sup>

<sup>1</sup>*School of Physics and Astronomy and Yunnan Key Laboratory for Quantum Information, Yunnan University, Kunming 650500, China*

<sup>2</sup>*Beijing Computational Science Research Center, Beijing 100193, People's Republic of China*

Recent proposals for building scalable quantum computational devices in semi-conductor based spin qubits introduce shared control lines in order to reduce the overhead of qubits controls. In principle, noises from the shared controls could introduce correlated errors to multi-qubit gates, and identifying them will be helpful for achieving higher gate fidelity in those setups. Here, we introduce a method based on the randomized benchmarking protocols that is capable of distinguishing among different correlated noises in a particular two-qubit model motivated by the crossbar architecture.

## I. INTRODUCTION

Fault-tolerant quantum computation requires synergy over a large number of physical qubits: Depending on the error rate, a logical qubit based on the surface code can take thousands of physical qubits to encode.<sup>1,2</sup> This motivates the construction of large scale quantum computational devices. Despite that single-qubit and two-qubit gates with the gate fidelity above the fault-tolerant threshold had been achieved across various platforms,<sup>3-5</sup> upto now only 72 qubits were realized experimentally based on the superconducting circuit,<sup>6</sup> and it was not until recently that the logical qubit could be demonstrated.<sup>7,8</sup>

One of the difficulties involved in building a desired large scale device capable of implementing error correction code is to maintain uniformity in the characteristic parameters across all the underlying qubits.<sup>9,10</sup> In this regard, semi-conductor based spin qubits stands out with a unique advantage of being compatible with the matured industrial fabrication technologies.<sup>11</sup> Following this approach, several proposals for building scalable devices had been put-forward.<sup>11-14</sup> Later in experiments, a two-dimensional crossbar array containing  $36 \times 36$  gates were reported,<sup>15</sup> while recently a two-dimensional array of 16 qubits with the inter-dot coupling above 10GHz was experimentally realized in terms of the SiGe based hole-spin quantum dots.<sup>16</sup>

Unlike the traditional few-qubit setups for the proof-of-principle demonstrations where each qubit could be individually addressable, those scalable proposals usually features common control lines that borrowed from the CMOS or crossbar architectures.<sup>11,13</sup> On one hand they reduce the complexity of control layers and enable the integration of plenty of qubits, on the other hand, however, the noises imposed on such shared control lines may affect several qubits at the same time, thus result in *correlated* errors among the qubits. Although cryo-CMOS techniques have been developed for the purpose of qubit operation,<sup>17,18</sup> since those noises differ from the influences of the local environment that experienced by individual qubit, it would be still useful to distinguish between those noises in order to further reduce the control errors that associated with the multi-qubit operations.

In this work, we explore several possible sources of correlated magnetic noises in a simplified two-qubit model motivated by the crossbar proposal for scalable quantum computation.<sup>13</sup> To distinguish among those noises, we apply a method based on the interleaved randomized benchmarking (IRB).<sup>19</sup> In addition to the standard random circuit in the IRB, we introduce an additional measurement induced decoherence process to selective address certain components of the noisy quantum channel. Although the investigation is based on a specific model, the method should be generally applicable also to other scenarios.

This paper is organized as follows: In Sec. II, we introduce the model and derive the magnetic field at the qubit location. In Sec. III, different possible magnetic noises are discussed, with the corresponding perturbative Hamiltonian given explicitly. In Sec. IV, the method based on the IRB is introduced and applied to distinguish between two particular correlated magnetic noises. Further discussions are provided in Sec. V, and we draw the conclusion in Sec. VI. Technique details can be found in the Appendices.

## II. MAGNETIC FIELD PROFILE

Following several papers about the proposal of crossbar architecture for salable quantum computation,<sup>11-13</sup> here we consider the following simplified model that schematically shown in FIG. 1(a). The system features an array of equally spacing parallel wires carrying currents in alternating directions. For an estimation of the magnetic field generated by the  $n$ -th wire at the qubit position, we use an effective media description such that<sup>20</sup>

$$\mathbf{b}_n = \frac{\mu_{\text{eff}} I}{2\pi r_n^2} \mathbf{e}_n \times \mathbf{r}_n, \quad (1)$$

where  $\mu_{\text{eff}}$  is the effective permeability of the media,  $I$  is the current through the  $n$ -th wire with the current direction indicated by the unit vector  $\mathbf{e}_n$ .  $\mathbf{r}_n$  is the position vector in the  $x$ - $z$  plane jointing from the wire to the spin qubit. The total magnetic field experienced by the qubit then amounts to the sum over the individual contribu-

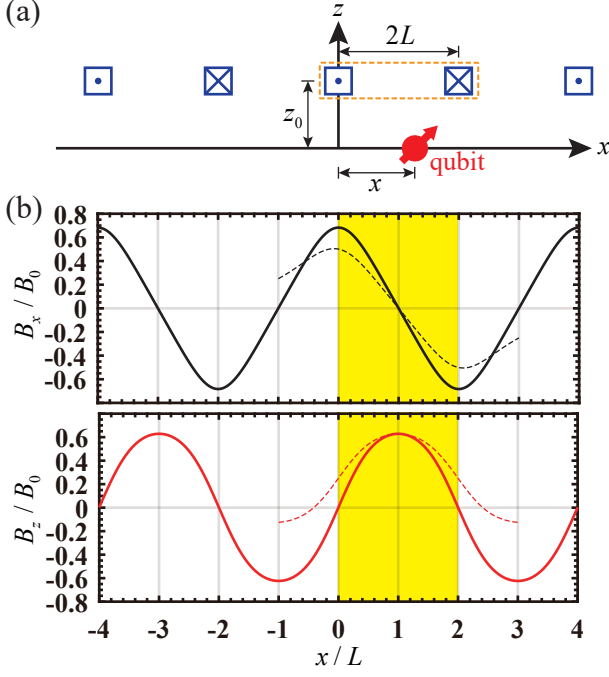


Figure 1. (a) Schematic plot of a spin qubit subjected to magnetic field that generated from parallel wires carrying alternating d.c. current. (b) The total magnetic field as a function of the qubit location. Solid curves are calculated from Eq. (3) with a cut-off 100 for the  $n$  summation, the dashed curves are obtained from the two nearest wires [highlighted by the dashed orange box in (a)] with a calibration coefficient, cf. Eq. (9). In above calculation we have assumed  $z_0 = L$  for clarity, while for  $z_0 \ll L$  the agreement between the solid and dashed curves will be improved.

tions from each wire

$$\mathbf{B} = \sum_n \mathbf{b}_n, \quad (2)$$

Specifically, for a qubit located at  $(x, 0, 0)$  under the configuration of FIG. 1(a), the total magnetic field is given by

$$\mathbf{B} = B_x \mathbf{e}_x + B_z \mathbf{e}_z, \quad (3)$$

$$B_x = B_0 \sum_{n=-\infty}^{\infty} \left( \frac{z_0^2}{r_{n,1}^2} - \frac{z_0^2}{r_{n,2}^2} \right), \quad (4)$$

and

$$B_z = B_0 \sum_{n=-\infty}^{\infty} \left( \frac{z_0 x_{n,1}}{r_{n,1}^2} - \frac{z_0 x_{n,2}}{r_{n,2}^2} \right). \quad (5)$$

Here,  $B_0 = \mu_{\text{eff}} I / (2\pi z_0)$  is the magnetic field generated by a single wire provided that the qubit is located right below the wire with the distance  $z_0$ .  $r_{n,j} = \sqrt{x_{n,j}^2 + z_0^2}$  and  $x_{n,j}$  with  $j = 1, 2$  are defined respectively as follows:

$$x_{n,1} = x - 4Ln, \quad x_{n,2} = x - 2L(2n + 1). \quad (6)$$

The magnetic field profile calculated according to Eq. (3) is shown in FIG. 1(b). In particular, the magnetic field in the  $z$  direction is insensitive to the qubit position near the center between adjacent wires, i.e., odd multiples of  $L$ . Therefore, the frequency of the qubit that operated at such locations will be insensitive to the qubit's displacements along  $x$  to the first order.<sup>13</sup> The exact sum in Eq. (3) can be carried out, giving the magnetic field at those ideal operation points  $x_k \equiv (2k + 1)L$  as follows

$$\mathbf{B}(x_k) = (-1)^k B_0 \zeta \text{sech} \zeta \mathbf{e}_z, \quad (7)$$

where the dimensionless quantity  $\zeta = \pi z_0 / (2L)$ . Similarly, one can also obtain the magnetic field at  $x = 2kL$  as

$$\mathbf{B}|_{x=2kL} = (-1)^k B_0 \zeta \text{csch} \zeta \mathbf{e}_x, \quad (8)$$

which provides the  $B_x$  noise insensitive operation points for the qubit.

If the qubit is located away from  $x_k$ , provided that  $z_0 \ll L$  and  $|x - x_k| \ll L$  then simplification for the magnetic field at the qubit location can be still made. This is achieved by restricting the sum over  $n$  in Eq. (3) to the nearest two wires [cf. the orange dashed box in FIG. 1(a)]. To ensure the agreement between the overall magnitude for  $B$  at the ideal operation point  $x = x_k$ , one could introduce a calibration coefficient which we take as  $\lambda_k = B(x_k) / [b_{k,1}(x_k) + b_{k,2}(x_k)]$ , such that

$$\mathbf{B}(x) \simeq \lambda_k \sum_{j=1,2} \mathbf{b}_{k,j}(x), \quad \text{for } x \simeq x_k. \quad (9)$$

Here,  $\mathbf{b}_{n,j}$  is obtained from Eq. (1) by replacing  $\mathbf{r}_n$  and  $\mathbf{e}_n$  with  $\mathbf{r}_{n,j}$  and  $\mathbf{e}_{n,j} \equiv (-1)^{j-1} \mathbf{e}_y$ , respectively. In FIG. 1(b), we also show the magnetic field for  $k = 0$  calculated from this approximation.

### III. MODEL AND THE SOURCE OF CORRELATED MAGNETIC NOISES

In order to implement two-qubit gates in a crossbar architecture, spins are usually shuttled close to each other such that their mutual exchange interaction can induce entanglement among the spin qubits.<sup>13</sup> In this sense, current fluctuations in a shared control wire, or a shift of the qubits positions due to mutual charge interaction, acts as a source of noise in the two-qubit operation but in a correlated way. Our goals in this section is to provide a description of such correlated noise at the Hamiltonian level.

The standard model for two-spin qubits operating in the (1,1) charge configuration is well known,<sup>21,22</sup> which can be described by the following Hamiltonian upto an overall constant

$$\hat{H} = J \hat{\mathbf{S}}_1 \cdot \hat{\mathbf{S}}_2 + \frac{1}{2} \left[ \omega \left( \hat{S}_1^z + \hat{S}_2^z \right) + \delta \omega \left( \hat{S}_1^z - \hat{S}_2^z \right) \right], \quad (10)$$

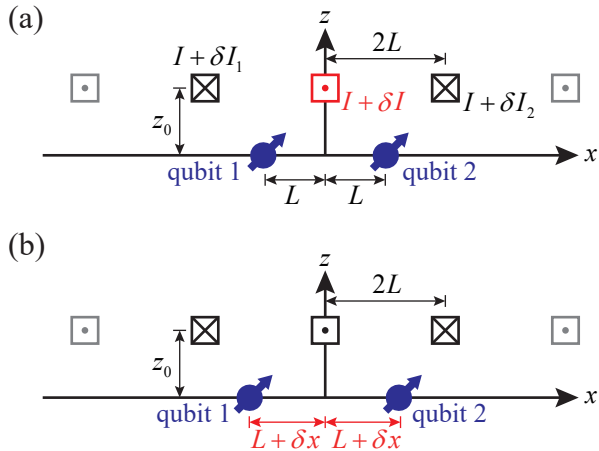


Figure 2. Two examples of correlated magnetic noise. (a) Change of the current at the central wire (highlighted in red) from  $I$  to  $I + \delta I$  causes related magnetic field perturbations at the location of qubit 1 and qubit 2. While the independent change of the currents at the two side wires by  $\delta I_1$  and  $\delta I_2$  induces uncorrelated magnetic field perturbations. (b) Mutual charge repulsion shifts the qubits locations by  $\delta x$  in a correlated way, thus the magnetic fields at the new locations differs from the original values that experienced by the qubits.

where  $J$  is the exchange interaction which depends on the tunneling coupling as well as the detuning between the two spin qubits,  $\omega = \omega_1 + \omega_2$  and  $\delta\omega = \omega_1 - \omega_2 + \delta\omega_{\text{cor}}$  are the sum as well as the difference of local Zeeman splittings  $\omega_1$  and  $\omega_2$  at the two qubits locations, while  $\delta\omega_{\text{cor}}$  is a correction due to the mixture of different charge states.<sup>23</sup>

The local Zeeman splittings  $\omega_1$  and  $\omega_2$  could be affected in a correlated way, e.g., when the noisy source acts on the both qubits. To be more specific, let us consider the configurations shown in FIG. 2 where the two spin qubits are shuttled next to each other in a row along the  $x$ -axis, typical for implementing controlled phase operation or spin-to-charge conversion.<sup>13</sup> As analyzed in the previous section, we shall focus on the magnetic fields generated only by the nearest wires [cf. FIG. 1(b)]. Thus the Zeeman splittings for the two qubits in the absence of noises are

$$\omega_1 = -2 \frac{g\mu_B B_0}{\hbar} \frac{z_0^2}{L^2 + z_0^2}, \quad \omega_2 = 2 \frac{g\mu_B B_0}{\hbar} \frac{z_0^2}{L^2 + z_0^2}. \quad (11)$$

Here,  $g$  is the  $g$ -factor for the spin qubit,  $\mu_B$  is the Bohr magneton, and the angle  $\theta = \arctan z_0/L$ . In general, the perturbation Hamiltonian through the mechanisms shown in FIG. 2 could be written into the following form,

$$\delta\hat{H} = \delta\omega_x (\hat{S}_1^x + \hat{S}_2^x) - \delta\omega_z (\hat{S}_1^z - \hat{S}_2^z), \quad (12)$$

while the specific values  $\delta\omega_x$  and  $\delta\omega_z$  depend on the details of the noisy scenarios. For the case of FIG. 2(a) with

a perturbation  $\delta I$  on the central wire, they are given by

$$\delta\omega_x = \frac{g\mu_B \delta B_0}{\hbar} \frac{z_0^2}{L^2 + z_0^2}, \quad \delta\omega_z = \frac{g\mu_B \delta B_0}{\hbar} \frac{z_0 L}{L^2 + z_0^2}, \quad (13)$$

and  $\delta B_0 = \mu_{\text{eff}} \delta I / (2\pi z_0)$ . Instead, for the position shifts scheme as shown in FIG. 2(b), the values are

$$\delta\omega_x = \frac{g\mu_B B_0}{\hbar} \left[ \frac{z_0^2}{(L + \delta x)^2 + z_0^2} - \frac{z_0^2}{(L - \delta x)^2 + z_0^2} \right], \quad (14)$$

$$\delta\omega_z = \frac{g\mu_B B_0}{\hbar} \left[ \frac{z_0(L + \delta x)}{(L + \delta x)^2 + z_0^2} + \frac{z_0(L - \delta x)}{(L - \delta x)^2 + z_0^2} \right]. \quad (15)$$

For comparison, if the current fluctuations  $\delta I_1$  and  $\delta I_2$  on the two side wires colored in black in FIG. 2(a) act independently from each other, the resulting perturbation Hamiltonian would be

$$\delta\hat{H} = -\delta\omega_{x,1} \hat{S}_1^x - \delta\omega_{x,2} \hat{S}_2^x - \delta\omega_{z,1} \hat{S}_1^z + \delta\omega_{z,2} \hat{S}_2^z, \quad (16)$$

where

$$\delta\omega_{\alpha,i} = \delta\omega_{\alpha}|_{\delta B_0 = \delta B_i}, \quad (17)$$

for  $i = 1, 2$  and  $\alpha = x, z$ , while  $\delta B_i = \mu_{\text{eff}} \delta I_i / (2\pi z_0)$ . Because here the noise is not due to a correlated source, thus the perturbation Eq. (16) is formally different from Eq. (12), expect for special situations, e.g.  $\delta I_1 = \delta I_2$  or  $\delta I_1 = -\delta I_2$ , where the perturbation Eq. (16) coincide with the form of the correlated perturbation.

#### IV. REVEAL THE EFFECTS OF CORRELATED NOISES BY RANDOMIZED BENCHMARKING

In the presence of noises, the actual implementation of a quantum gate deviates from the ideal one and this usually degrades the gate fidelity. However, in the context of highly integrated device implementation with shared controls where the noisy source could affects several qubits at the same time, it would be more useful to reveal the structure, e.g., the correlation, of the underlying noises instead of knowing the gate fidelity alone.

In this section, we investigate the correlated noisy effects of the model configuration in FIG. 2(a) by the interleaved randomized benchmarking (IRB).<sup>19</sup> Our scheme is illustrated in FIG. 3, where in addition to the standard circuit implementing the IRB. We introduced a measurement process  $\Lambda_M$  in between the random Clifford gates and the gate of interest  $\hat{U}_c$ . By chosen the basis for the measurement process, certain components of the noisy channel could be selected, such that one can distinguish between the two particular cases  $\delta I_1 = \delta I_2$  and  $\delta I_1 = -\delta I_2$  based on the scenario of FIG. 2(a), here we refer them as the *correlated* and the *anti-correlated* noisy perturbations.

For simplicity, we shall assume that in the ideal case  $\hat{U}_c$  is also an element from the two-qubit Clifford group  $\mathcal{C}_2$ .

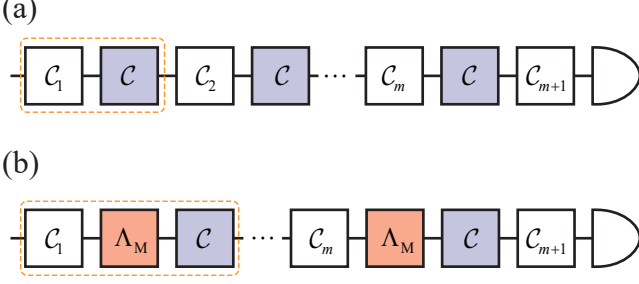


Figure 3. (a) Gate sequence in the interleaved benchmarking protocol (IRB), where  $\mathcal{C}_i$  is random two-qubit Clifford gate and  $\mathcal{C}$  is the gate of interest. After a sequence of  $m$  random evolution unit, the last gate  $\mathcal{C}_{m+1}$  reverts the effect of all previous gates, such that the measurement at the end of the gate sequence yields a result corresponding to the initial state with unit probability in the absence of noisy effects. (b) The modified IRB protocol, where a measurement process described with the quantum channel  $\Lambda_M$  is applied after each random Clifford gate.

This can be achieved from time evolution of the Hamiltonian  $\hat{H}$  with the following conditions:<sup>23</sup>

$$t = \pi J^{-1}, \quad \delta\omega = \sqrt{15}J, \quad \omega = 4kJ, \quad (18)$$

where  $k$  is any positive integer. With the above conditions, in the computational basis one has

$$\hat{U}_c = e^{-i\hat{H}t} = e^{-i\pi/4} \begin{bmatrix} 1 & 0 & 0 & 0 \\ 0 & i & 0 & 0 \\ 0 & 0 & i & 0 \\ 0 & 0 & 0 & 1 \end{bmatrix}, \quad (19)$$

which belongs to  $\mathcal{C}_2$  up to an overall phase factor.

The actually implemented gate of interest (denoted as  $\hat{U}$ ) evolves from the full Hamiltonian  $\hat{H} + \delta\hat{H}$  and, in the presence of magnetic noises, it deviates from  $\hat{U}_c$ . The associated effect of the gate error on time evolution can be formally written in terms of a quantum channel  $\Lambda_c$  given by

$$\Lambda_c[\rho] = \delta\hat{U}\hat{\rho}\delta\hat{U}^\dagger, \quad (20)$$

where  $\delta\hat{U} = \hat{U}_c^\dagger\hat{U}$ . Thus the time evolution of the actual gate is written as  $\hat{U}\hat{\rho}\hat{U}^\dagger = \mathcal{C} \circ \Lambda_c[\rho]$  with  $\mathcal{C}[\rho] = \hat{U}_c\rho\hat{U}_c^\dagger$ .

Following the standard approach (see also Appendix A for a brief review),<sup>19,24</sup> we prepared the two-qubit system in the initial state  $|\uparrow, \uparrow\rangle$  and performed the usual randomized benchmarking (RB) to extract the depolarization parameter  $p$  associated with noise channel  $\Lambda$  for the random Clifford gates. For simplicity, we assume a gate independent noise channel  $\Lambda$  such that the zero-th order fitting model is applicable to extract  $p$ . Then by interleaving the actual implementation of  $\hat{U}_c$  in between each random Clifford gate [cf. FIG. 3(a)], one obtains a modified depolarization parameter  $p_c$  that associates

with the combined noisy channel  $\Lambda_c \circ \Lambda$ . From  $p_c$  and  $p$  the average error rate of  $\Lambda_c$  could be estimated from<sup>19</sup>

$$r_c^{\text{est}} = \frac{d-1}{d} \left(1 - \frac{p_c}{p}\right), \quad (21)$$

where  $d$  is the dimension of the Hilbert space. In the absence of noises for implementing the random Clifford gates,  $p = 1$  and Eq. (21) reduces to the well known RB result  $(d-1)(1-p_c)/d$ .<sup>24,25</sup>

From the above approach, the average error rate for the actual implementation of the gate  $\hat{U}_c$  is simulated and shown in FIG. 4(a). The result suggests that  $r_c^{\text{est}}$  obtained from the standard IRB is symmetric with respect to rotations in the  $\delta I_1$ - $\delta I_2$  plane, i.e.,  $r_c^{\text{est}}$  depends only on  $\sqrt{\delta I_1^2 + \delta I_2^2}$ . This is more clearly seen by comparing the two special cases with  $\delta I_1 = \delta I_2$  and  $\delta I_1 = -\delta I_2$  as shown in the lower panel of FIG. 4(a), where the calculated  $r_c^{\text{est}}$  overlaps with each other, even though those two cases represent completely different correlations among the perturbations applied to the side wires [cf. FIG. 2(a)].

To better distinguish between the *correlated* and the *anti-correlated* cases, we modify the gate sequence in the standard IRB protocol, which is illustrated in FIG. 3(b). As mentioned before, the main difference here is to introduce a measurement induced decoherence process, given in term of a noisy channel  $\Lambda_M[\rho] = \hat{P}\hat{\rho}\hat{P}^\dagger + \hat{Q}\hat{\rho}\hat{Q}^\dagger$ , where  $\hat{P}$  and  $\hat{Q}$  are complementary projection operators satisfying  $\hat{P} + \hat{Q} = \hat{I}$ . Introducing  $\Lambda_M$  is motivated by the fact that the insensitive of the standard IRB circuit to  $\delta I_1$  and  $\delta I_2$  could be related to the symmetry of the perturbation Hamiltonian. In particular, one can show that for the perturbation term  $\delta\hat{H}$  given by Eq. (16), there are two dark states for each of the two special cases, i.e.,  $\delta\hat{H}_\lambda|D_i\rangle_\lambda = 0$  with  $\lambda \in \{S, A\}$ , where  $\delta\hat{H}_\lambda$  is defined as follows

$$\delta\hat{H}_S = \delta\hat{H}|_{\delta I_1=\delta I_2}, \quad \delta\hat{H}_A = \delta\hat{H}|_{\delta I_1=-\delta I_2}. \quad (22)$$

The specific form of those dark states are listed in the Appendix B. Furthermore, the projectors  $\hat{P}_{\lambda,i} = |D_i\rangle_\lambda\langle D_i|$  satisfy  $\hat{P}_{S,i}\hat{P}_{A,j} = 0$ . Therefore, projection with  $\hat{P}_{S,i}$  ( $\hat{P}_{A,i}$ ) during the implementation of the random circuit will reduce the effects of noisy perturbation in the *anti-correlated* (*correlated*) case and lead to higher sequence fidelity, thus enables the distinguishing between the two situations.

Based on the scheme of FIG. 3(b), the sequence fidelity from a particular realization of the random circuit becomes

$$F_{\text{seq}} = \text{Tr} \left\{ \hat{E}_\xi \Lambda \circ \mathcal{C}_{m+1} \left[ \prod_{i=1}^m \mathcal{C} \circ \Lambda_c \circ \Lambda_M \circ \Lambda \circ \mathcal{C}_i \right] \hat{\rho}_0 \right\}, \quad (23)$$

where  $\mathcal{C}_{m+1} = [\prod_{i=1}^m \mathcal{C} \circ \mathcal{C}_i]^{-1}$ . Then by averaging  $F_{\text{seq}}$  over  $N_{\text{avg}}$  realizations over the random circuits, one has

$$\langle F_{\text{seq}} \rangle = \text{Tr} \left\{ \hat{E}_\xi \Lambda \circ [\Lambda_c \circ \Lambda_M \circ \Lambda]_d^m \hat{\rho}_0 \right\} \equiv A p_c^m + B, \quad (24)$$

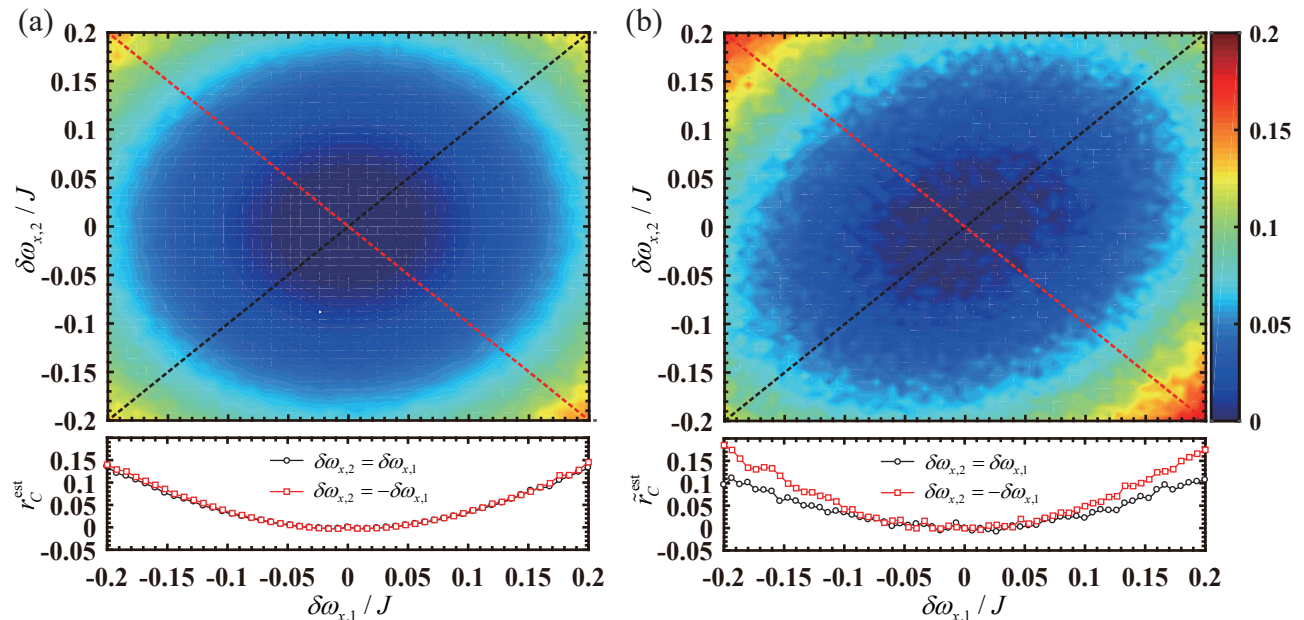


Figure 4. (a) Main panel: average error rate  $r_C^{\text{est}}$  associated with the actual implementation of the two-qubit gate  $\hat{U}_c$  subjected to independent noises  $\delta I_1$  and  $\delta I_2$ , which are proportional to the Zeeman splittings according to Eqs.(13,17). The error rate is obtained from the standard IRB protocol. Lower panel:  $r_C^{\text{est}}$  along the black and red dashed cuts in the main panel. (b) Main panel: The error rate  $\tilde{r}_C^{\text{est}}$  extracted from the modified protocol as in FIG. 3(b), lower panel:  $\tilde{r}_C^{\text{est}}$  along the black and red cuts of the main panel. Here, we choose the initial state  $|\uparrow, \uparrow\rangle$  for simulation, and  $\hat{P} = |\text{T}_0(1, 1)\rangle\langle\text{T}_0(1, 1)|$  for constructing  $\Lambda_M$ . Parameters used in the calculation:  $t = \pi/J$ ,  $\omega = 20J$ ,  $\delta\omega = \sqrt{15}J$ ,  $z_0 = L$ ,  $N_{\text{avg}} = 10^3$ ,  $m = 200$  in (a) and  $m = 30$  in (b).

where  $\tilde{p}_c$  is the depolarization parameter associated with the combined depolarization noisy channels  $[\Lambda_c \circ \Lambda_M \circ \Lambda]_d$ , after taking the twirling operation over the two-qubit Clifford group.<sup>24,26</sup> Alternatively, removing  $\mathcal{C} \circ \Lambda_c$  from Eq. (23) provides a circuit that gives rise to a referential value for the sequence fidelity, whose average leads to the depolarization parameter  $\tilde{p}$  associated with  $[\Lambda_M \circ \Lambda]_d$ . Thus by inserting  $\tilde{p}$  and  $\tilde{p}_c$  into Eq. (21), one can extract another error rate  $\tilde{r}_C^{\text{est}}$  associated with gate of interest.

With properly chosen basis for the measurement related projection operator  $\hat{P}$ , the error rate  $\tilde{r}_C^{\text{est}}$  could distinguish between the *correlated* and *anti-correlated* noises cases. This is shown in FIG. 4(b) for  $\hat{P} = |\text{T}_0(1, 1)\rangle\langle\text{T}_0(1, 1)|$ , where  $|\text{T}_0(1, 1)\rangle$  is the triplet state  $|\uparrow, \downarrow\rangle + |\downarrow, \uparrow\rangle$  and also one of the dark states for  $\delta\hat{H}_A$ . Here, the error rate shows asymmetry as  $\delta I_1$  and  $\delta I_2$  varying, and the error rate grows more slowly for the *correlated* noise perturbation as  $\delta I_1$  and  $\delta I_2$  increasing.

## V. DISCUSSIONS

Although here we only analysis through a particular perturbation  $\delta\hat{H}$  that described by the configuration of FIG. 2(a), the idea of introducing measurement induced decoherence to distinguish noisy correlations should be also applicable to other types of noisy sources, for example, apart from alternating current-carrying wires, other

way of generating the magnetic field gradient include the use of micromagnets,<sup>27,28</sup> as well as the Overhauser fields from polarized nuclear spins.<sup>29,30</sup> However, in order to construct  $\tilde{r}_C^{\text{est}}$  that will be sensitive to the noisy correlation, the proper choice of projection operators  $\hat{P}$  and  $\hat{Q}$  are crucial. To find out those operators, one may wish to enable simpler calculation instead of the full IRB simulations. In fact, we found similar asymmetry behavior in the depolarization parameter  $\tilde{p}_c$  of  $[\Lambda_c \circ \Lambda_M \circ \Lambda]_d$ . Notice that this is directly related to the twirling of  $\Lambda_c \circ \Lambda_M \circ \Lambda$  under the two-qubit Clifford group. Thus for theoretical analysis, it is useful to first consider  $[\Lambda_c \circ \Lambda_M \circ \Lambda]_d$  instead of  $\tilde{r}_C^{\text{est}}$ .

The sequence fidelity depends also on the system initial state, thus choosing proper initial state could be also useful to distinguish the noisy correlations. For example, suppose the initial state of the two-qubit system is  $|\text{T}_0(1, 1)\rangle \propto |\uparrow, \downarrow\rangle + |\downarrow, \uparrow\rangle$ , since this state is also a dark state of  $\delta\hat{H}_A$  [cf. Eq. (B3)], thus calculating with this initial state amounts to applying the projection operator  $\hat{P}$  at the beginning and end of the random circuit. Throughout the calculation we have assumed that the two-qubit system is prepared in the  $|\uparrow, \uparrow\rangle$  state. For spin qubits based on the double quantum dot, this state can be prepared by adiabatically changing the detuning through the S-T<sub>+</sub> anti-crossing that induced with the transverse field of micromagnet.<sup>31,32</sup>

For the purpose of illustration, we did not apply real-

istic parameters in the simulation. In silicon based double quantum dot, the exchange coupling above 10MHz had been measured,<sup>33</sup> while for the crossbar system, the magnetic field was designed such that  $\delta\omega \sim 10\text{MHz}$  and  $\omega \sim 100\text{MHz}$ .<sup>13</sup> Also, the calculations were performed in the absence of qubit relaxation or dephasing, and the dynamical aspect of the current fluctuation in  $\delta I_1$  and  $\delta I_2$  are ignored. The detailed treatment of those effects are out of the current scope and will be addressed in the future works.

## VI. CONCLUSIONS

In this paper, we have explored correlated magnetic noise in a two-qubit model stimulated by the recent proposals of scalable quantum computation in semiconductor based spin qubits. With the method introduced here, we could distinguish between the *correlated* and *anti-correlated* noisy cases from their different magnetic field dependence of the error rate, obtained from the interleaved randomized benchmarking protocol by using the modified random circuit. The key idea is to introduce a measurement based decoherence process such that certain component of the noisy channel associated with the correlated noise could be singled out.

## ACKNOWLEDGMENTS

Y.F. acknowledges support from NSFC (Grant No. 12005011) and Yunnan Fundamental Research Projects (Grant No. 202201AU070118).

### Appendix A: Interleaved randomized benchmarking

In this Appendix, we follow Refs.<sup>19,24,25,34</sup> to provide a brief summary of the interleaved randomized benchmarking (IRB) protocol.

In general, the protocol involves three steps: First perform the usual randomized benchmarking (RB) to extract  $p$ ;<sup>24,25,34</sup> Then perform an interleaved version of the random circuits to extract  $p_c$ ;<sup>19</sup> Finally, from  $p_c$  and  $p$  one obtain an estimate for the average error rate  $r_C^{\text{est}}$  associated with the gate of interest, given in terms of the average fidelity  $r_C^{\text{est}} = 1 - F_{\text{avg}}[\Lambda_c]$  associated with noisy channel to implement the gate of interest

$$F_{\text{avg}}[\Lambda_c] = \int d\psi \langle \psi | \Lambda_c[|\psi\rangle\langle\psi|] | \psi \rangle. \quad (\text{A1})$$

Next, we describe the above steps in more detail. In the first step, to extract  $p$  the sequence fidelity is calculated as a function of the number of random gates  $m$  applied to the circuit

$$F_{\text{seq}} = \text{Tr} \left\{ \hat{E}_\xi \Lambda \circ \mathcal{C}_{m+1} \left[ \prod_{i=1}^m \Lambda \circ \mathcal{C}_i \right] \hat{\rho}_0 \right\}, \quad (\text{A2})$$

where  $\hat{\rho}_0$  is the initial state,  $\hat{E}_\xi$  is the final measurement operator. In the absence of state preparing and measurement errors one could set  $\hat{\rho}_0 = |\psi_0\rangle\langle\psi_0|$  and also  $\hat{E}_\xi = |\psi_0\rangle\langle\psi_0|$ .  $\mathcal{C}_i[\hat{\rho}] = \hat{U}(g_i)\hat{\rho}\hat{U}(g_i)^\dagger$  with  $g_i \in \mathcal{C}_n$  being an element of the  $n$ -qubit Clifford group  $\mathcal{C}_n$ , while  $\Lambda$  is the gate-independent quantum channel describing the noisy effect involved in implementing the Clifford gate  $\mathcal{C}_i$ . Notice that there are only  $m$  random gates, which uniquely determines the last gate  $\mathcal{C}_{m+1} \equiv [\mathcal{C}_m \circ \dots \circ \mathcal{C}_1]^{-1}$ . Since  $F_{\text{seq}}$  is random because of  $\{\mathcal{C}_i\}$ . Thus one should consider the averaged quantity  $\langle F_{\text{seq}} \rangle$  by random sampling over the random Clifford gates, for sufficiently large number of samples  $N_{\text{avg}}$ , the averaged sequence fidelity approximates the following exact value

$$\langle F_{\text{seq}} \rangle \stackrel{\text{large } N_{\text{avg}}}{\simeq} \frac{1}{|\mathcal{C}_n|^m} \sum_{\mathcal{C}_1 \dots \mathcal{C}_m} F_{\text{seq}}. \quad (\text{A3})$$

Since the Clifford group form a unitary 2-design,<sup>26</sup> thus the discrete sum over the Clifford group element can reproduce the continuous average over  $\text{SU}(n)$  appeared in the definition of the average fidelity Eq. (A1). In particular, the twirling operation on  $\Lambda$  by the Clifford group yields a depolarization channel

$$[\Lambda]_{\text{tw}} \equiv \frac{1}{|\mathcal{C}_n|} \sum_{g \in \mathcal{C}_n} \mathcal{C}(g) \circ \Lambda \circ \mathcal{C}(g)^{-1} = [\Lambda]_{\text{d}}, \quad (\text{A4})$$

such that  $[\Lambda]_{\text{d}}\hat{\rho} = p\hat{\rho} + (1-p)\hat{I}/d$ , where  $p$  is known as the depolarization parameter. Importantly, due to the unitary 2-design property, the average fidelity of  $[\Lambda]_{\text{d}}$  is the same as that for  $\Lambda$ .<sup>19</sup> By the group rearrangement theorem,  $[\Lambda]_{\text{d}}$  commutes with arbitrary Clifford gate  $\mathcal{C}(g)$ , thus the average sequence fidelity follows simply the zeroth order fitting model given by<sup>25</sup>

$$\langle F_{\text{seq}} \rangle = Ap^m + B. \quad (\text{A5})$$

In the second step, to extract  $p_c$  one interleaves the gate of interest  $\hat{U}_c$  in between random Clifford gates, thus the sequence fidelity of the modified circuit becomes

$$F_{\text{seq},c} = \text{Tr} \left\{ \hat{E}_\xi \Lambda \circ \mathcal{C}_{m+1} \left[ \prod_{i=1}^m \mathcal{C} \circ \Lambda_c \circ \Lambda \circ \mathcal{C}_i \right] \hat{\rho}_0 \right\}, \quad (\text{A6})$$

where  $\mathcal{C}[\hat{\rho}] = \hat{U}_c\hat{\rho}\hat{U}_c^\dagger$  and  $\mathcal{C}_{m+1} = [\prod_{i=1}^m \mathcal{C} \circ \mathcal{C}_i]^{-1}$ . Similar consideration leads to the conclusion that the average sequence fidelity again follows the fitting model Eq. (A5) but with modified parameters

$$\langle F_{\text{seq},c} \rangle = Ap_c^m + B. \quad (\text{A7})$$

Now  $p_c$  is the depolarization parameter of  $[\Lambda_c \circ \Lambda]_{\text{d}}$ .

In the third step, one estimates  $r_C^{\text{est}}$  according to Eq. (21), which can be derived by identifying the average fidelity of  $\Lambda_c \circ \Lambda$  with that of  $\Lambda_c \circ [\Lambda]_{\text{d}}$ .<sup>19</sup>

## Appendix B: Dark states of $\delta\hat{H}$

Here, we list all the dark states for  $\delta\hat{H}_S$  and  $\delta\hat{H}_A$ , i.e., the perturbation term defined in Eq. (22). For  $\delta\hat{H}_S$  the two dark states are

$$|D_1\rangle_S = \frac{1}{\sqrt{2}} [|\uparrow, \uparrow\rangle - |\downarrow, \downarrow\rangle], \quad (\text{B1})$$

and

$$|D_2\rangle_S = \frac{1}{2} [|\uparrow, \uparrow\rangle - |\uparrow, \downarrow\rangle + |\downarrow, \uparrow\rangle + |\downarrow, \downarrow\rangle]. \quad (\text{B2})$$

While for  $\delta\hat{H}_A$  the two dark states are

$$|D_1\rangle_A = \frac{1}{\sqrt{2}} [|\uparrow, \downarrow\rangle + |\downarrow, \uparrow\rangle], \quad (\text{B3})$$

and

$$|D_2\rangle_A = \frac{1}{2} [|\uparrow, \uparrow\rangle + |\uparrow, \downarrow\rangle - |\downarrow, \uparrow\rangle + |\downarrow, \downarrow\rangle]. \quad (\text{B4})$$

- 
- \* ynfang@ynu.edu.cn
- <sup>1</sup> A. Fowler, M. Mariantoni, J. M. Martinis, and A. N. Cleland, *Phys. Rev. A* **86** (2012).
  - <sup>2</sup> J. Preskill, *Quantum* **2**, 79 (2018).
  - <sup>3</sup> C. J. Ballance, T. P. Harty, N. M. Linke, M. A. Sepiol, and D. M. Lucas, *Phys. Rev. Lett.* **117**, 060504 (2016).
  - <sup>4</sup> A. Noiri, K. Takeda, T. Nakajima, T. Kobayashi, A. Sammak, G. Scappucci, and S. Tarucha, *Nature* **601**, 338 (2022).
  - <sup>5</sup> X. Xue, M. Russ, N. Samkharadze, B. Undseth, A. Sammak, G. Scappucci, and L. M. K. Vandersypen, *Nature* **601**, 343 (2022).
  - <sup>6</sup> A. I. Google Quantum, *Nature* **614**, 676 (2023).
  - <sup>7</sup> Y. Zhao, Y. Ye, H.-L. Huang, Y. Zhang, D. Wu, H. Guan, Q. Zhu, Z. Wei, T. He, S. Cao, F. Chen, T.-H. Chung, H. Deng, D. Fan, M. Gong, C. Guo, S. Guo, L. Han, N. Li, S. Li, Y. Li, F. Liang, J. Lin, H. Qian, H. Rong, H. Su, L. Sun, S. Wang, Y. Wu, Y. Xu, C. Ying, J. Yu, C. Zha, K. Zhang, Y.-H. Huo, C.-Y. Lu, C.-Z. Peng, X. Zhu, and J.-W. Pan, *Phys. Rev. Lett.* **129**, 030501 (2022).
  - <sup>8</sup> S. Krinner, N. Lacroix, A. Remm, A. Di Paolo, E. Genois, C. Leroux, C. Hellings, S. Lazar, F. Swiadek, J. Herrmann, G. J. Norris, C. K. Andersen, M. Muller, A. Blais, C. Eichler, and A. Wallraff, *Nature* **605**, 669 (2022).
  - <sup>9</sup> A. Laucht, F. Hohls, N. Ubbelohde, M. F. Gonzalez-Zalba, D. J. Reilly, S. Stobbe, T. Schroder, P. Scarlino, J. V. Koski, A. Dzurak, C.-H. Yang, J. Yoneda, F. Kuemmeth, H. Bluhm, J. Pla, C. Hill, J. Salfi, A. Oiwa, J. T. Muhonen, E. Verhagen, M. D. LaHaye, H. H. Kim, A. W. Tsen, D. Culcer, A. Geresdi, J. A. Mol, V. Mohan, P. K. Jain, and J. Baugh, *Nanotechnology* **32**, 162003 (2021).
  - <sup>10</sup> M. Meyer, C. Deprez, T. R. van Abswoude, I. N. Meijer, D. Liu, C.-A. Wang, S. Karwal, S. Oosterhout, F. Borsoi, A. Sammak, N. W. Hendrickx, G. Scappucci, and M. Veldhorst, *Nano Lett.* **23**, 2522 (2023).
  - <sup>11</sup> M. Veldhorst, H. G. J. Eenink, C. H. Yang, and A. S. Dzurak, *Nat. Commun.* **8**, 1766 (2017).
  - <sup>12</sup> D. Hill Charles, P. Eldad, J. Hile Samuel, G. House Matthew, F. Martin, R. Sven, Y. Simmons Michelle, and L. Hollenberg Lloyd C., *Sci. Adv.* **1**, e1500707 (2015).
  - <sup>13</sup> R. Li, L. Petit, D. P. Franke, J. P. Dehollain, J. Helsen, M. Steudtner, N. K. Thomas, Z. R. Yoscovits, K. J. Singh, S. Wehner, L. M. K. Vandersypen, J. S. Clarke, and M. Veldhorst, *Sci. Adv.* **4**, eaar3960 (2018).
  - <sup>14</sup> M. F. Gonzalez-Zalba, S. de Franceschi, E. Charbon, T. Meunier, M. Vinet, and A. S. Dzurak, *Nat. Electron.* **4**, 872 (2021).
  - <sup>15</sup> P. L. Bavdaz, H. G. J. Eenink, J. van Staveren, M. Lodari, C. G. Almudever, J. S. Clarke, F. Sebasatiano, M. Veldhorst, and G. Scappucci, *npj Quantum Inf.* **8** (2022).
  - <sup>16</sup> F. Borsoi, N. W. Hendrickx, V. John, M. Meyer, S. Motz, F. van Riggelen, A. Sammak, S. L. de Snoo, G. Scappucci, and M. Veldhorst, *Nat. Nanotechnol.* (2023), 10.1038/s41565-023-01491-3.
  - <sup>17</sup> B. Patra, R. M. Incandela, J. P. G. van Dijk, H. A. R. Homulle, L. Song, M. Shahmohammadi, R. B. Staszewski, A. Vladimirescu, M. Babaie, F. Sebastiano, and E. Charbon, *IEEE J. Solid-State Circuits* **53**, 309 (2018).
  - <sup>18</sup> E. Charbon, M. Babaie, A. Vladimirescu, and F. Sebastiano, *IEEE Microwave Mag.* **22**, 60 (2021).
  - <sup>19</sup> E. Magesan, J. M. Gambetta, B. R. Johnson, C. A. Ryan, J. M. Chow, S. T. Merkel, M. P. da Silva, G. A. Keefe, M. B. Rothwell, T. A. Ohki, M. B. Ketchen, and M. Steffen, *Phys. Rev. Lett.* **109**, 080505 (2012).
  - <sup>20</sup> J. D. Jackson, *Classical Electrodynamics* (John Wiley & Sons, Inc., United States, 1999).
  - <sup>21</sup> G. Burkard, *Phys. Rev. B* **60**, 11404 (1999).
  - <sup>22</sup> T. Meunier, V. E. Calado, and L. M. K. Vandersypen, *Phys. Rev. B* **83**, 121403 (2011).
  - <sup>23</sup> Y. Fang, arXiv: 2312.12892v1 (2023).
  - <sup>24</sup> E. Magesan, J. M. Gambetta, and J. Emerson, *Phys. Rev. A* **85**, 042311 (2012).
  - <sup>25</sup> E. Magesan, J. M. Gambetta, and J. Emerson, *Phys. Rev. Lett.* **106**, 180504 (2011).
  - <sup>26</sup> C. Dankert, R. Cleve, J. Emerson, and E. Livine, *Phys. Rev. A* **80**, 012304 (2009).
  - <sup>27</sup> Y. Tokura, W. G. van der Wiel, T. Obata, and S. Tarucha, *Phys. Rev. Lett.* **96**, 047202 (2006).
  - <sup>28</sup> M. Pioro-Ladriere, T. Obata, Y. Tokura, Y.-S. Shin, T. Kubo, K. Yoshida, T. Taniyama, and S. Tarucha, *Nat. Phys.* **4**, 776 (2008).
  - <sup>29</sup> J. Baugh, Y. Kitamura, K. Ono, and S. Tarucha, *Phys. Rev. Lett.* **99**, 096804 (2007).
  - <sup>30</sup> J. Baugh, Y. Kitamura, K. Ono, and S. Tarucha, *Phys. Status Solidi C* **5**, 302 (2008).
  - <sup>31</sup> X. Wu, D. R. Ward, J. R. Prance, D. Kim, J. K. Gamble, R. T. Mohr, Z. Shi, D. E. Savage, M. G. Lagally, M. Friesen, S. N. Coppersmith, and M. A. Eriksson, *Proc. Natl. Acad. Sci.* **111**, 11938 (2014).

- <sup>32</sup> S. Chesi, Y.-D. Wang, J. Yoneda, T. Otsuka, S. Tarucha, and D. Loss, *Phys. Rev. B* **90**, 235311 (2014).
- <sup>33</sup> M. Veldhorst, C. H. Yang, J. C. C. Hwang, W. Huang, J. P. Dehollain, J. T. Muhonen, S. Simmons, A. Laucht, F. E. Hudson, K. M. Itoh, A. Morello, and A. S. Dzurak, *Nature* **526**, 410 (2015).
- <sup>34</sup> J. Emerson, R. Alicki, and K. Życzkowski, *J. Phys. B At. Mol. Opt.* **7**, s347 (2005).